Probing physicochemical properties of a mixed-anion protic ionic liquid based on [TFSI] and [NO3]

Journal of Molecular Liquids 437 (2025) 128418

Contents lists available at ScienceDirect

Journal of Molecular Liquids

journal homepage: www.elsevier.com/locate/molliq

Probing physicochemical properties of a mixed-anion protic ionic liquid based on [TFSI] and [NO_3]

Nicole Abdou [a,*], Achilleas Pipertzis [b], Jan Swenson [b], Anna Martinelli [a,*]

[a] Department of Chemistry and Chemical Engineering, Chalmers University of Technology, Gothenburg, SE-412 96, Sweden
[b] Department of Physics, Chalmers University of Technology, Gothenburg, SE-412 96, Sweden

ARTICLE INFO

Keywords:
Protic ionic liquid
Mixed-anion
Electrolytes
Phase behavior
Ion dynamics
Spectroscopy

ABSTRACT

Mixtures comprising two protic ionic liquids, both having the same cation but different anions, 1-ethylimidazolium bis(trifluoromethylsulfonyl)imide and 1-ethylimidazolium nitrate, were systematically investigated as a function of composition, here defined by the molar fraction of bis(trifluoromethylsulfonyl)imide anion present in the mixture. To assess their potential as electrolytes for lithium-ion batteries, samples containing lithium bis(trifluoromethanesulfonyl)imide salt (0.2 M) were also studied. In order to provide a thorough characterization, phase behavior, density, viscosity, ionic conductivity, and intermolecular interactions were all analyzed. This work provides insights into the structure–property correlation in these mixed ionic liquid systems and their suitability for energy storage applications.

1. Introduction

The development of sustainable energy storage devices, including batteries, is crucial in today's world as society faces increasing environmental challenges. One important factor influencing battery performance is the choice of electrolyte. Among various options, ionic liquids emerge as promising electrolytes due to their unique and tunable properties, *i.e.,* high chemical and thermal stability, good ionic conductivity, and a broad electrochemical stability window [1,2]. Ionic liquids are molten salts with a melting temperature below 100 °C and can be categorized into various subclasses based on their chemical structure, the most common being protic, aprotic and zwitterionic ionic liquids [3,4]. Protic ionic liquids are formed by a straightforward neutralization reaction between a Brønsted acid and a Brønsted base [5,6]. This reaction involves an exchangeable proton that is typically located on the cation, generating donor and acceptor sites that facilitate the formation of hydrogen bonds. Hence, protic ionic liquids have been extensively explored for the exchange of protons in intermediate temperature fuel cells, but also as electrolytes in other electrochemical devices such as Li-ion batteries and supercapacitors [7–9].

A key limitation for the use of ionic liquids is the occurrence of phase transitions close to the operating temperature of the devices, which directly affects their performance. To address this challenge, counteracting strategies like nano-confinement, co-solvent addition, and mixing have been investigated [10–14]. In this context, Miran et al. have studied mixtures consisting of diethylmethylammonium hydrogensulfate ([dema][HSO_4]) and diethylmethylammonium bis(trifluoromethanesulfonyl)amide ([dema][TFSI]), where the anions were derived from acids of different strength (*i.e.*, different pK_a values) [15]. This study revealed that the hydrogen bonding between the [HSO_4] anion and the [dema] cation was stronger than between [TFSI] and the [dema] cation. As a result of the complex hydrogen bonds formed in the mixtures, the authors also reported a proton transport mechanism that extends beyond the vehicular transport only, in fact including both the vehicular and the Grotthuss mechanism. On the same line, Abdurrokhman et al. investigated the impact of combining two protic ionic liquids, 1-ethylimidazolium triflate [C_2Him][TfO] and 1-ethylimidazolium bis(trifluoromethylsulfonyl)imide [C_2Him][TFSI], on the phase behavior, intermolecular interactions, and ionic conductivity of the resulting systems [16]. The authors observed a broader liquid phase range with the addition of the [TFSI]-based ionic liquid, accompanied by enhanced conductivity and lower viscosity. These effects were attributed to weaker [Im]···[TFSI] interactions and increased molecular-level disorder. Moreover, Tang and coworkers considered the impact of mixing n-butylammonium acetate and n-butylammonium nitrate on the intermolecular dynamics within the systems [17]. They observed stronger hydrogen bonding between n-butylammonium and the nitrate anion compared to acetate, resulting in easier proton transfer in the case of

* Corresponding authors.
E-mail addresses: nicole.abdou@chalmers.se (N. Abdou), anna.martinelli@chalmers.se (A. Martinelli).

https://doi.org/10.1016/j.molliq.2025.128418
Received 2 July 2025; Received in revised form 8 August 2025; Accepted 27 August 2025

Available online 10 September 2025

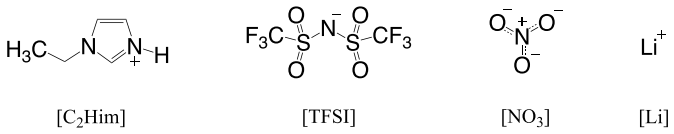

Fig. 1. Molecular structure of the 1-ethylimidazolium [C_2Him] and the lithium [Li] cations as well as of the bis(trifluoromethylsulfonyl)imide [TFSI] and the nitrate [NO_3] anions.

acetate. Timperman et al. also explored the use of a blend of two protic ionic liquids, pyrrolidinium nitrate [Pyrr][NO_3] and pyrrolidinium bis(trifluoromethylsulfonyl) imide [Pyrr][TFSI], aiming to create amorphous electrolytes for energy storage systems [18]. The authors reported eutectic mixtures for $0.1 \leq \chi_{[Pyrr][NO_3]} \leq 0.72$, an increased conductivity upon increasing the [Pyrr][NO_3] mole fraction and promising electrochemical properties.

In this study, mixtures of imidazolium-based protic ionic liquids containing two different anions, *i.e.*, bis(trifluoromethylsulfonyl)imide [TFSI] and nitrate [NO_3], were systematically investigated with focus on their phase behavior, intermolecular interactions, and transport properties. The anions were selected for their specific advantages in Li-ion battery systems; [TFSI] for its high electrochemical stability, [19,20] and [NO_3] for its ability to promote the formation of a stable solid-electrolyte interphase (SEI) layer, essential for efficient Li^+ transport [21,22]. In addition, mixtures containing 0.2 M of lithium bis(trifluoromethanesulfonyl)imide (LiTFSI) salt were examined as potential electrolytes for Li-ion batteries.

2. Experimental

2.1. Materials

The protic ionic liquids 1-ethylimidazolium bis(trifluoromethylsulfonyl)imide ([C_2Him][TFSI]) (V001x102.1.2-IL-0269), 98% purity, and 1-ethylimidazolium nitrate ([C_2Him][NO_3]) (Q00168.1-IL-0272), 98% purity, were purchased from Iolitec. The salt lithium bis(trifluoromethanesulfonyl)imide (LiTFSI) (99.95% trace metal basis) was purchased from Sigma-Aldrich. All chemicals were stored in an N_2 filled glovebox (MBRAUN UNIlab Plus Eco glovebox, equipped with an MB-LMF II solvent absorber system; ≤ 1 ppm H_2O; ≤ 1 ppm O_2) and used as received without further treatment. The molecular structures of the ions in the two protic ionic liquids and the lithium salt are given in Fig. 1. The two protic ionic liquids were mixed at different molar ratios, resulting in binary mixtures with different mole fractions, χ_{TFSI}, of [C_2Him][TFSI] with $0.0 \leq \chi_{TFSI} \leq 1.0$. Ternary mixtures containing 0.2 M LiTFSI were also examined. All samples were prepared in the glovebox to prevent moisture absorption and were taken out just before characterization.

2.2. Methods

2.2.1. Calorimetric measurements

Differential Scanning Calorimetry (DSC) measurements were performed using a Q2000 TA Instruments calorimeter, equipped with a liquid nitrogen cooling system (LNCS). Samples of a mass between 10 and 14 mg were encapsulated in a hermetic aluminum crucible. An empty aluminum crucible was used as a reference. The temperature protocol began with a rapid cooling scan to -120 °C at a rate of 20 °C/min, followed by a heating scan up to 60 °C at 10 °C/min, under nitrogen flow. Two cycles were recorded for each measurement. The glass transition temperature (T_g) was determined using a sigmoid function, while the melting temperature (T_m) was taken from the endothermic peak observed in the second heating scan. Prior to the measurement, the calorimeter was calibrated to ensure optimal performance. The pre-calibration procedure involved (*i*) cleaning of the cell, (*ii*) conditioning the cell to create an inert atmosphere using helium gas, and (*iii*) calibrating the LNCS baseline. Subsequently, a three-point calibration using indium (T_m = 155.8 °C, ΔH_m = 28.71 J/g), mercury (T_m = -38.68 °C, ΔH_m = 11.443 J/g) and MilliQ water (T_m = 0.15 °C, ΔH_m = 335 J/g) was carried out for the calibration of the enthalpy and transition temperatures. Finally, a baseline measurement was conducted with an empty cell to confirm the successful calibration of the instrument. Regarding the heat capacity calibration, a temperature-modulated DSC (TM-DSC) calibration was carried out using a sapphire standard.

2.2.2. Dielectric spectroscopy

Conductivity and relaxation data were collected using a Novocontrol GmBH broadband dielectric spectrometer. The liquid mixtures were placed into a parallel plate sample cell (BDS 1308) equipped with stainless steel electrodes. A uniform thickness of 100 μm was maintained using Teflon spacers. Measurements were conducted in the frequency range from 10^{-2} to 10^7 Hz, covering the temperature range -100 °C to 150 °C. Data were measured every 5 °C with a stabilization time of 600 s at each temperature. A low voltage electric field of 0.01 V was employed to reduce electrode polarization effects. The temperature was controlled using a nitrogen gas cryostat, with a stability of 0.1 °C.

2.2.3. Viscosity and density

Viscosity and density measurements were measured using an Anton Paar DMA 4500 M oscillation U-tube densitometer from 20 °C to 80 °C with temperature steps of 5 °C. Viscosity measurements were performed using a Lovis 2000 ME rolling ball viscometer module. The temperature accuracy is ±0.02 °C, with a repeatability of ±0.005 °C. The viscosity measurement has an accuracy of up to 0.1%, and a repeatability up to 0.5%. The density accuracy is approximately ±0.00001 g/cm^3.

2.2.4. Raman spectroscopy

Raman spectra were recorded using a Renishaw InVia Reflex Raman spectrophotometer equipped with an air-cooled CCD detector and using a 785 nm wavelength diode laser as the excitation source. The combination of this monochromatic light with a 1200 grooves/mm grating provided a spectral resolution about 1 cm^{-1}. The laser power was set to 10% of its maximum value, which is nominally 300 mW at the source. Before the Raman measurements, the mixture samples were sealed in NMR tubes inside a glovebox to avoid moisture absorption. The Raman spectra were collected at ambient conditions, covering the 100-4000 cm^{-1} spectral range. Recorded spectra were accumulated by 10 scans with an acquisition time of 10 s each. Before each measurement, the spectrophotometer was calibrated to the first-order vibrational mode of a Si wafer centered at 520.6 cm^{-1}. The raw Raman spectra were treated by excluding sharp signals coming from cosmic rays. For further analysis, and to estimate integrated areas, a multipeak fit procedure based on a linear background and Voigt functions was applied, to selected spectral regions, using the Igor Pro 9 software. In the fitting procedure, the width and position of the Voigt components were not subjected to any constraint.

2.2.5. Infrared spectroscopy

Infrared spectra were collected using an Alpha II Bruker infrared spectrometer in the ATR (Attenuated Total Reflection) mode using a single-reflection diamond crystal. The measurements were conducted inside a glovebox to prevent moisture absorption. Spectra were acquired over the 400-4000 cm^{-1} spectral range with 128 accumulations hence achieving a spectral resolution of 2 cm^{-1}.

2.2.6. NMR spectroscopy

Qualitative ^{1}H NMR data were collected using a Bruker Avance 600 MHz NEO spectrometer. The ionic liquid samples were loaded into 3 mm NMR tubes, each containing a capillary filled with DMSO-d6 solvent. The NMR tubes were filled and sealed in a glovebox using a PTFE sealing tape. The data were collected at 25 °C. The pulse angle was set to 90°, the relaxation delay was set to 5 s and 64 scans were collected.

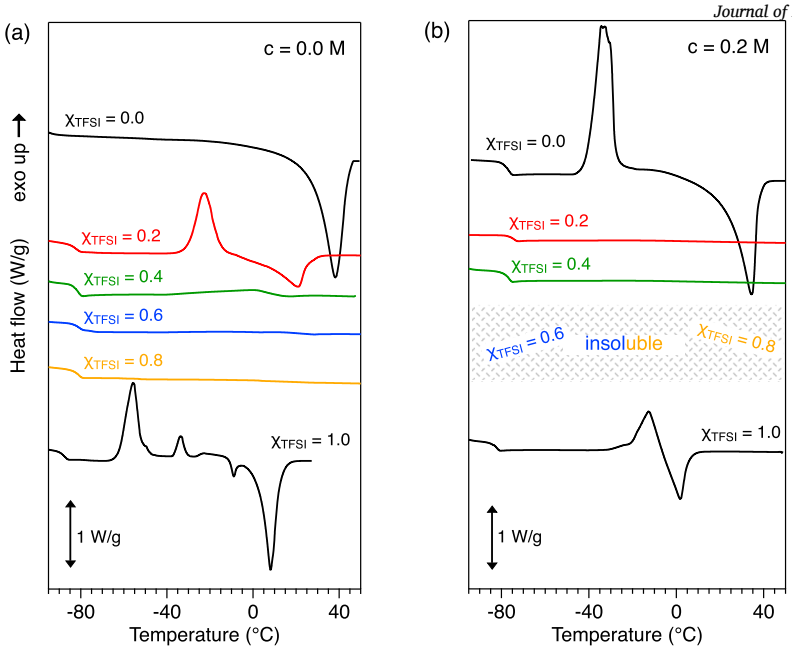

Fig. 2. DSC thermograms of the bulk and mixed protic ionic liquids; (a) c = 0.0 M LiTFSI (b) c = 0.2 M LiTFSI. The DSC traces shown are those recorded during the second heating scan, with a heating rate of 10 °C/min. The thermograms are shown with a vertical offset for clarity.

3. Results and discussion

3.1. Phase behavior

The thermodynamic properties and phase behavior of the protic ionic liquid mixtures, with and without Li salt, were studied by DSC. Most of the DSC traces shown in Fig. 2a show glass transition temperatures, T_g, below -70 °C, associated with the amorphous domains in the samples. At higher temperatures, first-order phase transitions are observed. The neat [C_2Him][NO_3] shows a melting peak near 38 °C, while neat [C_2Him][TFSI] exhibits a glass transition around -83 °C, followed by cold crystallization and then melting transitions.

Moreover, mixing the two ionic liquids results in broader and less sharp peaks, as observed for χ_{TFSI} = 0.2, and ultimately suppresses the phase transitions for 0.4 ≤ χ_{TFSI} ≤ 0.8, turning these mixtures into strong glass-forming liquids. Upon adding Li salt (Fig. 2b), the phase behavior displays some changes. The χ_{TFSI} = 0.0 solution ([C_2Him][NO_3] with 0.2 M LiTFSI), exhibits a glass transition followed by cold crystallization and melting. As also reproduced in Fig. 3, the solid-liquid transitions are inhibited in the mixtures with χ_{TFSI} = 0.2 and χ_{TFSI} = 0.4, while a limited solubility of LiTFSI is observed in the mixtures with χ_{TFSI} = 0.6 and χ_{TFSI} = 0.8. Also, the addition of LiTFSI increases T_g by 5–10 °C (Fig. 3, bottom plot), which is attributed to a higher viscosity as reported in previous studies [19,23]. The melting and glass transition temperature values for all samples can be found in the Supporting Information, Table S1. To summarize, both the anion mixing and the addition of LiTFSI have an effect on the phase behavior of these mixtures.

3.2. Density and viscosity

Density and viscosity are important properties of ionic systems, as they are highly sensitive to temperature and are critically connected to transport properties. Accordingly, density and viscosity of the bulk ionic liquids and of their mixtures were measured at variable temperatures ranging from 20 °C to 80 °C, Fig. 4. The densities of the mixtures (Fig. 4a) increase continuously with χ_{TFSI} (filled symbols). The addition of LiTFSI salt leads to a further increase in the densities of the mixtures (open symbols). It is important to note that salt-containing mixtures with χ_{TFSI} = 0.6 and 0.8 could not be prepared due to the limited solubility of the Li salt. A linear fit was applied to the density data to determine how the density changes with temperature across different compositions. The fits confirm a higher slope, hence a stronger temperature dependence, for increased χ_{TFSI} values (Figure S1). This suggests reduced intermolecular interactions within the system as χ_{TFSI} increases, which facilitated thermal expansion. Furthermore, viscosity reveals a small compositional dependence close to room temperature, decreasing exponentially with temperature to converge into a similar value at high temperatures (Fig. 4b). All density and viscosity values are summarized in Tables S2-S3 in the SI.

At constant temperature, the viscosity of the mixtures initially increases, up to χ_{TFSI} = 0.2, followed by a smooth decrease reaching a minimum at χ_{TFSI} = 1.0 (Fig. 5a,b).

3.3. Ion transport mechanism

The transport properties of the studied ionic mixtures were investigated using dielectric spectroscopy. Fig. 5c and d show the ionic conductivity of the binary mixtures (0.0 ≤ χ_{TFSI} ≤ 1.0), with and without LiTFSI and for temperatures between -10 °C and 80 °C. For comparison, the Arrhenius plots of all samples can be found in the Supporting In-

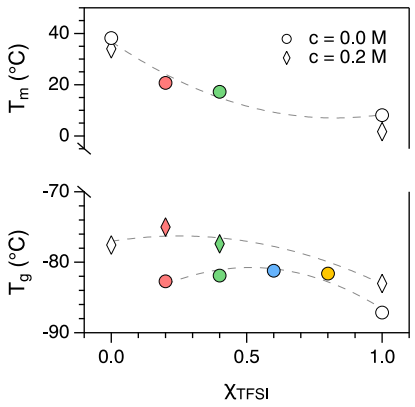

Fig. 3. Melting (upper panel) and glass transition (lower panel) temperatures for neat ionic liquids and ionic liquid mixtures without (circles) and with (diamonds) LiTFSI. The errors extracted from the fitting of the DSC curves are smaller than the symbols.

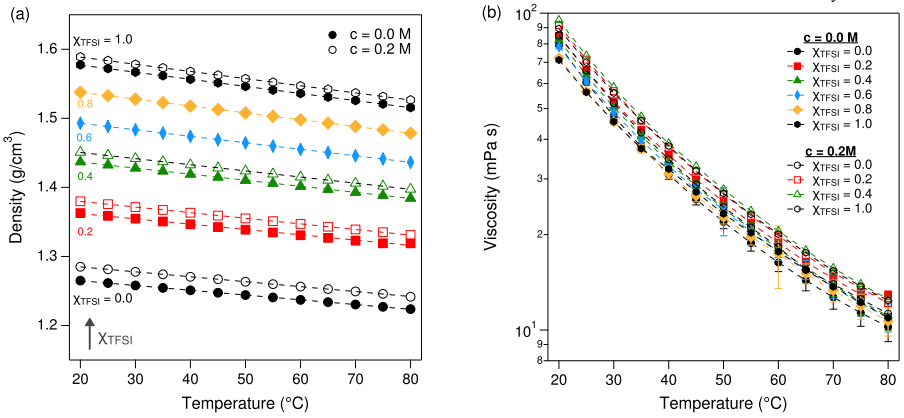

Fig. 4. Density (a) and viscosity (b) as a function of temperature of all binary and ternary systems.

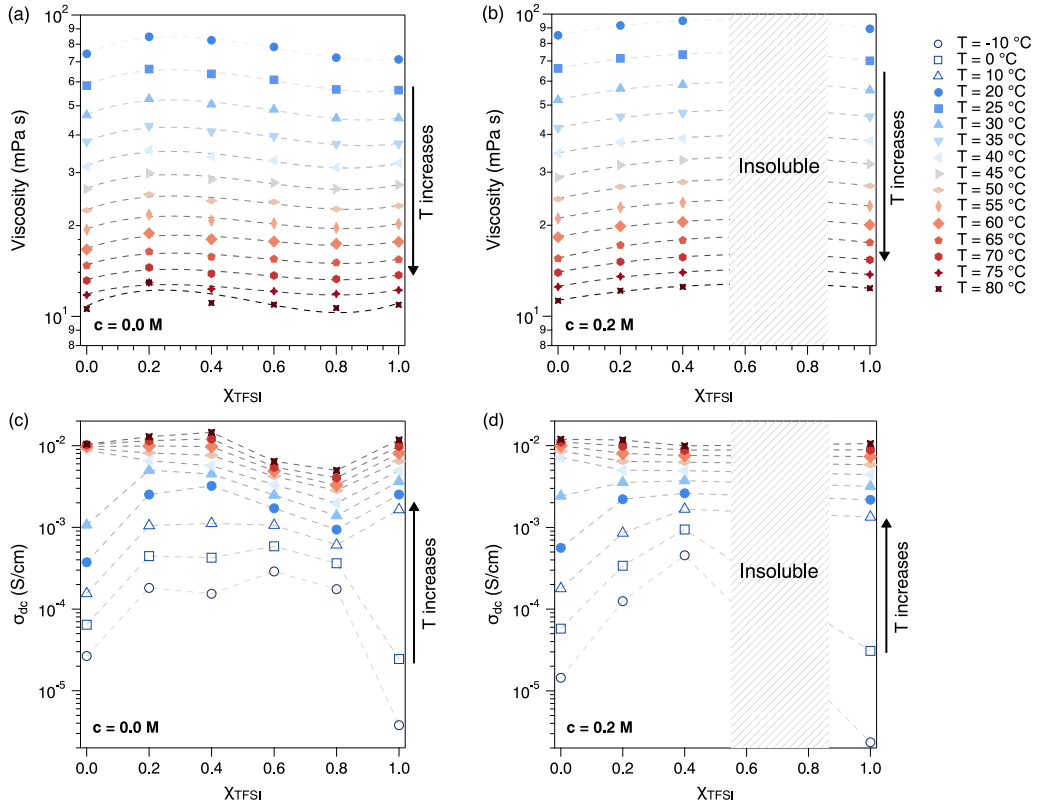

Fig. 5. Composition dependence (χ_{TFSI}) on viscosity (a) without and (b) with added LiTFSI and on ionic conductivity (c) without and (d) with LiTFSI at different temperatures. The same temperature color coding is used in all four figures.

formation (Figure S2). The ionic conductivity values were extrapolated from the plateau of the frequency dependent spectra (Figure S3).

The ionic conductivity of neat [C_2Him][NO_3] exhibits a discontinuity between 30 and 40 °C, attributed to melting by comparison to the DSC curve. Likewise, the conductivity of [C_2Him][TFSI] shows a similar disruption near its melting temperature of 7 °C. For temperatures below 40 °C, the ionic conductivity increases significantly with the addition of [C_2Him][TFSI] (χ_{TFSI} = 0.2). However, as χ_{TFSI} increases further ($0.4 \leq \chi_{TFSI} \leq 0.8$), the conductivity remains very little affected. For temperatures above 40 °C, the conductivity values remain nearly unchanged for most compositions, except for $0.6 \leq \chi_{TFSI} \leq 0.8$, where a notable decrease is observed. This significant drop may be attributed to strong intermolecular interactions or the formation of aggregates. There is however, no evidence for these hypotheses other than the insolubility of the salt at these same compositions as also marked in Fig. 5.

With the addition of salt (Fig. 5d), similar trends were observed. However, interestingly, the ionic conductivity for χ_{TFSI} = 0.4 appears higher in the presence of salt, possibly due to the complete suppression of first-order transitions as confirmed by DSC. Overall, although the [TFSI] anion has a higher molar mass than [NO_3], the ionic conductivity of the mixtures increases with [TFSI] addition.

To gain further insight into the differences in ion association between the ionic systems, the measured conductivity, density and viscosity were used to construct Walden plots, as shown in Fig. 6. In a Walden plot, the relationship between molar conductivity and fluidity is plotted,[1] with

[1] $\Lambda_m \eta^\gamma$ = C. γ is a constant $0 \leq \gamma \leq 1$. $\Lambda_m = \sigma_{dc} \cdot V_m = \sigma_{dc} \cdot M_w / \rho$, where σ_{dc} is the specific conductivity, V_m is the molar volume, M_w is the molar mass and ρ is the density.

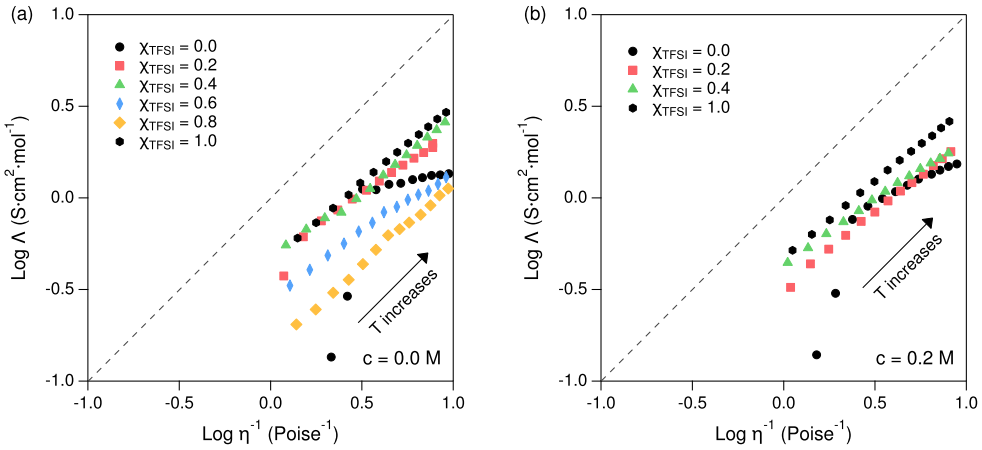

Fig. 6. Walden plot of the studied mixtures (a) c = 0.0 M LiTFSI, (b) c = 0.2 M LiTFSI.

reference to an ideal system, namely a 0.01 M KCl aqueous solution, in which the ions are considered to be fully dissociated. The degree of deviation from the ideal line is accepted as a measure of ion association. Furthermore, the slope of the curves reflects the response of the systems to temperature changes. The Walden plots for all studied mixtures fall below the ideal line, indicating the presence of aggregates or incomplete ionic dissociation. Upon mixing, the deviation from the ideal line initially decreases for compositions with χ_{TFSI} = 0.2 and 0.4, followed by a sharp increase for χ_{TFSI} = 0.6 and 0.8, before decreasing again to reach the minimum deviation for χ_{TFSI} = 1.0. This indicates that the degree of ion association varies with the composition, suggesting that specific mixing ratios (χ_{TFSI} = 0.2, 0.4) between the two ionic liquids can enhance the system's transport properties. The slope of χ_{TFSI} = 0.0 deviates noticeably from those of the other compositions, suggesting a unique response of this system to temperature variation. Moreover, the addition of salt (Fig. 6b) leads to a slight increase in the deviation from the ideal line, without affecting the overall trend previously discussed, *i.e.*, ion association decreases as χ_{TFSI} increases.

3.4. Ionic interactions and local coordination

The experimentally recorded Raman spectra of the binary mixtures based on [C_2Him][NO_3] and [C_2Him][TFSI] are shown in Fig. 7, normalized to the intensity of the vibration observed at 961 cm^{-1} that is assigned to the C-C stretching in the ethyl chain of [C_2Him] [24]. As a consequence of this normalization, the strong signatures of the [NO_3] anion (1041 cm^{-1}) and the [TFSI] anion (741 cm^{-1}) decrease and increase, respectively, with the increased molar fraction of [C_2Him][TFSI] (see also the guiding arrows in the Fig. 7). Both these features are sensitive to the anion's environment and their frequency can be used as an indication of the strength of the established anion-cation interaction. The main component of the peak at 1041 cm^{-1}, for instance, blue shifts upon interactions with increasingly smaller (hence more charge dense) cations, as reported previously by Kocevska et al. [25]. An equivalent trend has been found for the characteristic feature of [TFSI] observed at 741 cm^{-1}; [26] hence, these interaction sensitive signatures can be used to better understand [TFSI] and [NO_3] based ionic materials. A peak fitting analysis has been employed to the Raman spectra in order to get an exact estimate of the peaks' position and thus elucidate the effect of the mixed anions on their respective state of coordination.

A number of peak fitted spectra in the region of the [TFSI] feature are reproduced in Fig. 8 for χ_{TFSI} varying from 0.0 to 1.0, while the fitting procedure in the range where the [NO_3] stretching appears is given in Figure S4. In the frequency region 720–770 cm^{-1} our fitting model includes two components that account for the co-existing conformers of [TFSI], *cis* and *trans*. These components are less than 2 cm^{-1} apart within the range 741–743 cm^{-1}, in agreement with their calculated positions [27]. Moreover, none of the Raman spectra (with or without the Li salt) show a high-frequency component at ~745 cm^{-1}, which would indicate the presence of strongly coordinated [TFSI]-[Li] complexes [28]. As summarized in the left-side bottom panel of Fig. 8, the main component at 741 cm^{-1} red shifts upon addition of [C_2Him][NO_3]

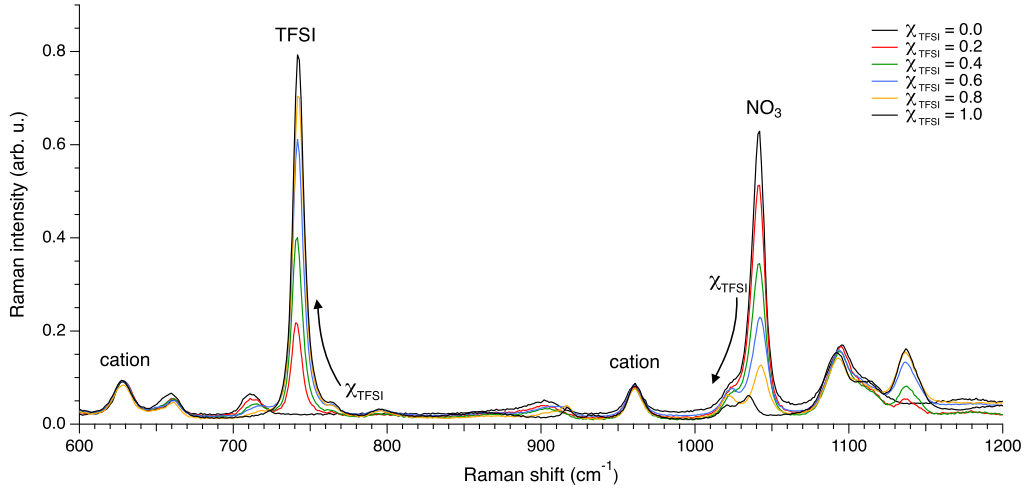

Fig. 7. Normalized Raman spectra collected at room temperature for the binary mixtures ($0.0 \leq \chi_{TFSI} \leq 1.0$) in the 600–1200 cm^{-1} range.

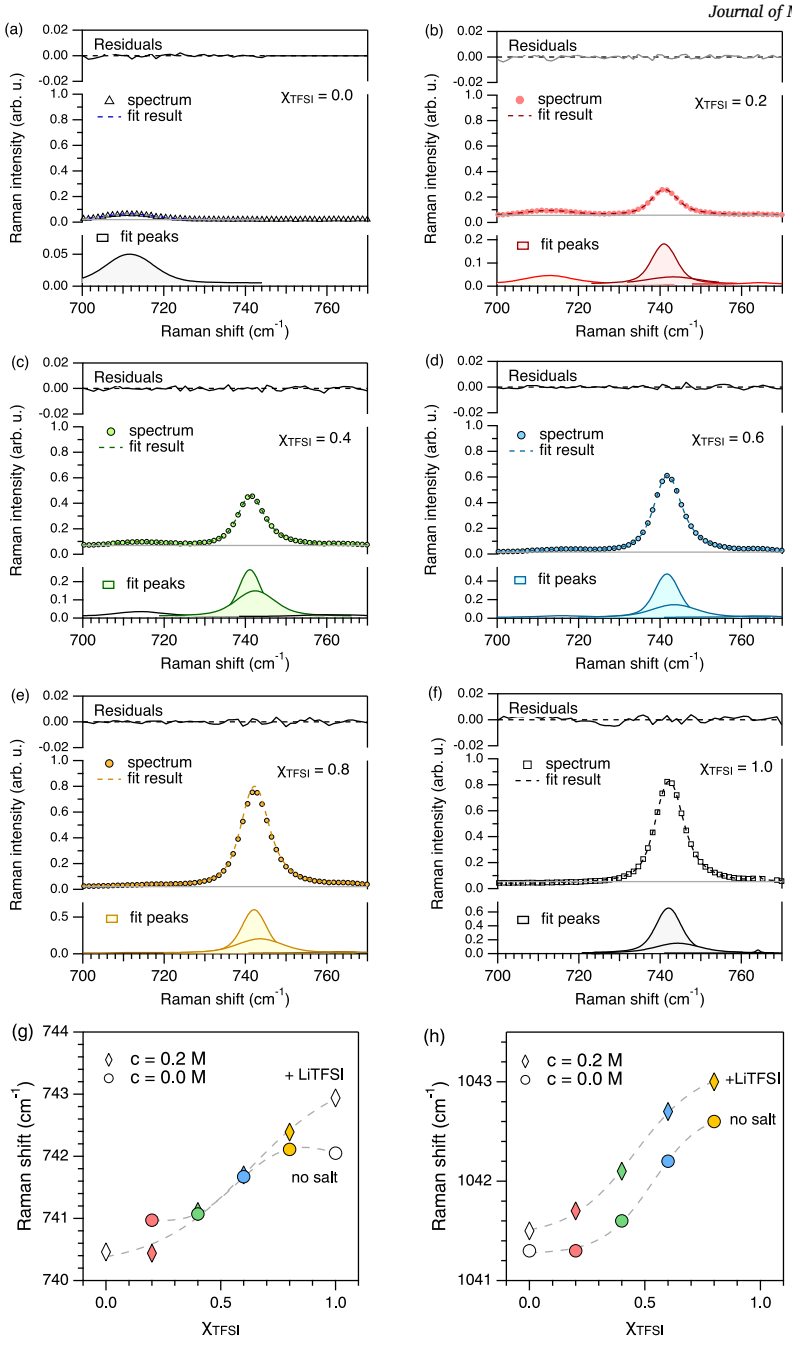

Fig. 8. The first six panels show the experimentally recorded Raman spectra (symbols), the fitting peaks (colored Voigt profiles), the fit results (dashed lines) and the residuals (black line) for all binary mixtures (c = 0.0 M). The bottom most panels show the position of the fitting peaks as a function of composition for the [TFSI] (left) and the [NO_3] (right) characteristic peaks, showing the two cases of pure solutions (diamonds) and 0.2 M solutions of LiTFSI (circles).

to [C_2Him][TFSI] (*i.e.*, for decreasing values of χ_{TFSI}). Also, the blue shift typically observed when a Li salt is added to an ionic liquid is suppressed in these mixtures. It is important to recall that the salt was not soluble in the χ_{TFSI} = 0.6 and 0.8 solutions, as previously mentioned, and only the liquid phase was analyzed by Raman to gain a rough insight into the interactions in these mixtures.

In previous studies of aqueous solutions of nitrate salts, the broad NO stretching mode appearing in the range 1020–1080 cm^{-1} has been deconvoluted into several components, distinguishing between free [NO_3] anions and solvent-shared or contact ion pairs [25]. In the Raman spectra of the mixtures, the [TFSI] anion has a marginal contribution between 1020 and 1040 cm^{-1} (see Figure S5). Our fitting model is thus based on two contributions, one at ~1028 cm^{-1} which accounts for the weak contributions of both [NO_3] and [TFSI] and a major one at ~1041 cm^{-1} attributed to 'free' [NO_3] anions. Additional peaks at the higher frequency flank, which would have been attributed to contact ion pairs, were not needed in the fitting procedure. The right-side bottom panel in Fig. 8 reveals a blue shift for the Raman feature at ~1041 cm^{-1} as [C_2Him][TFSI] is added to [C_2Him][NO_3] (*i.e.* for increasing values of χ_{TFSI}). This trend is also observed upon addition of the Li salt, with an additional up-shift of the vibrational frequencies.

Altogether, these observations reveal that in the ionic solutions with mixed anions, the counter-cations [C_2Him] and [Li] preferably interact with the [NO_3] anions, leaving the [TFSI] anions in weaker interactions. We emphasize that these are small yet clearly measurable trends. Similar observation has previously been reported by Abdurokhman and coworkers for binary systems consisting of [C_2Him][TFSI] and [C_2Him][TfO] protic ionic liquids [16]. The authors reported (*i*) a

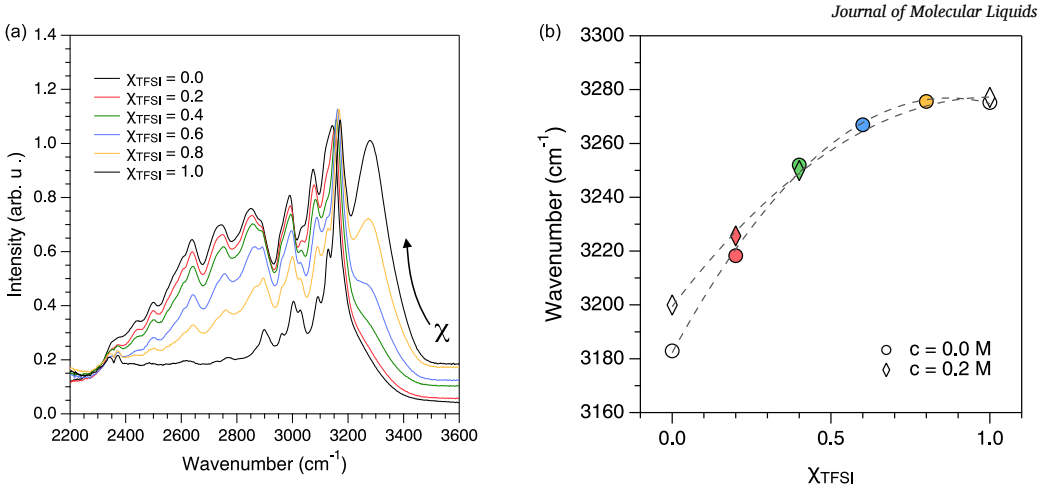

Fig. 9. (a) Infrared spectra recorded for the binary mixtures in the 2200–3600 cm^{-1} frequency range. (b) The frequency of the NH stretching mode as a function of composition.

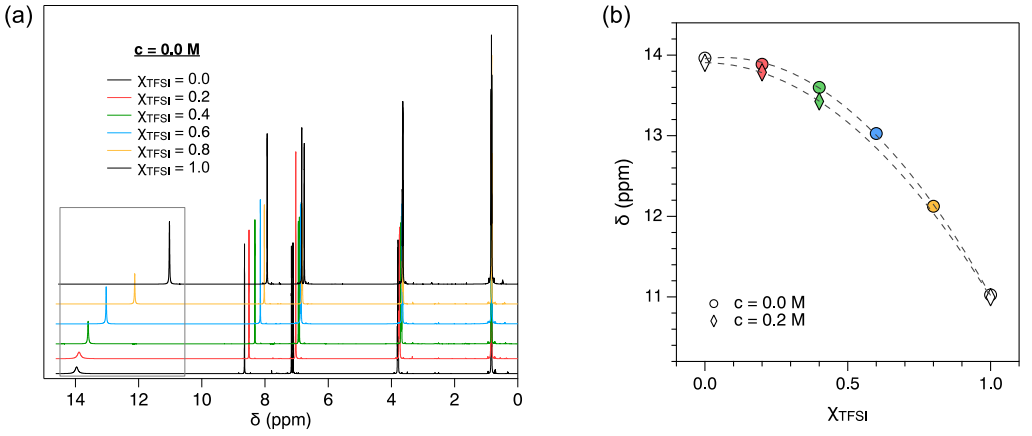

Fig. 10. (a) ^{1}H NMR spectra of all binary mixtures and bulk ILs at room temperature. (b) ^{1}H NMR chemical shift of the N(H) peak as a function of composition.

red shift of the [TFSI] Raman signature mode at 742 cm^{-1} and (*ii*) a red shift of the N-H stretching mode observed by infrared, upon addition of [C_2Him][TfO] (decreasing χ_{TFSI}). These observations were attributed to stronger [C_2Him]...[TfO] interactions *via* NH bonding, hence weaker interactions between [TFSI] and its surroundings.

To gain further insights into cation-anion interactions, in particular hydrogen bond formation, the infrared spectra were used to analyze the cation's N-H stretching. Fig. 9a shows the infrared spectra of all mixtures (c = 0.0 M) within the 2200–3600 cm^{-1} spectral range. All spectra shown are normalized to the mode at 1580 cm^{-1}, which corresponds to the in-plane deformations of the imidazolium ring and remains independent of the anion type. The spectral range in Fig. 9a includes C-H stretching modes of the ethyl chain (2200–3200 cm^{-1}) and the N-H stretching mode of the imidazolium ring (3200–3500 cm^{-1}). The N-H stretching mode exhibits a strong, distinct peak for [C_2Him][TFSI] but red shifts and broadens as χ_{TFSI} decreases, approaching the case of pure [C_2Him][NO_3]. To delve deeper into spectral evolution, a detailed peak fitting of the 2200–3600 cm^{-1} range was performed using Voigt functions and a linear background, leaving the fitting parameters unconstrained. An example of the fitting can be found in the supporting information in Figure S6. The peak fitting analysis reveals an average blue shift of the N-H stretching frequency with increasing χ_{TFSI}, reflecting a shorter N-H bond. This observation may be attributed to on average weaker cation–anion interactions in the [TFSI] rich systems relative to the [NO_3] rich ones.

Further understanding of the local interactions between cations and anions was obtained by examining the ^{1}H chemical shifts in the NMR spectra. As the χ_{TFSI} concentration was increased, the N(H) proton signals shifted to lower resonance frequencies, while the signals of the other ring protons showed minimal shifts and the alkyl proton signals remained largely unchanged, Fig. 10a. The frequency of the N–H infrared stretching mode and the ^{1}H NMR chemical shift values are provided in Table S4 of the Supporting Information. A shift to higher resonance frequencies in NMR is typically associated with increased deshielding effects, often due to hydrogen bonding with electronegative groups. Therefore, the observed shielding of the N(H) protons, shown in Fig. 10b, indicates that hydrogen bonding between the cation and anion becomes weaker in the [TFSI] rich liquids. This interpretation is consistent with the blue shift observed in the infrared spectra and supports the conclusion that [C_2Him] cation preferably interact with [NO_3], resulting in weaker interactions with [TFSI].

3.5. Relaxation dynamics

A comprehensive insight into ion and molecular dynamics was obtained by combining dielectric spectroscopy, TM-DSC, and rheology methods data acquired across a broad range of frequencies and temperatures. Dielectric spectroscopy allows the determination of the characteristic relaxation time (τ_σ) for ion transport, which is identified from the peak position of the imaginary component of the electric modulus (M'') as:

$$\tau_\sigma = \frac{1}{2\pi f_{max}} \quad (1)$$

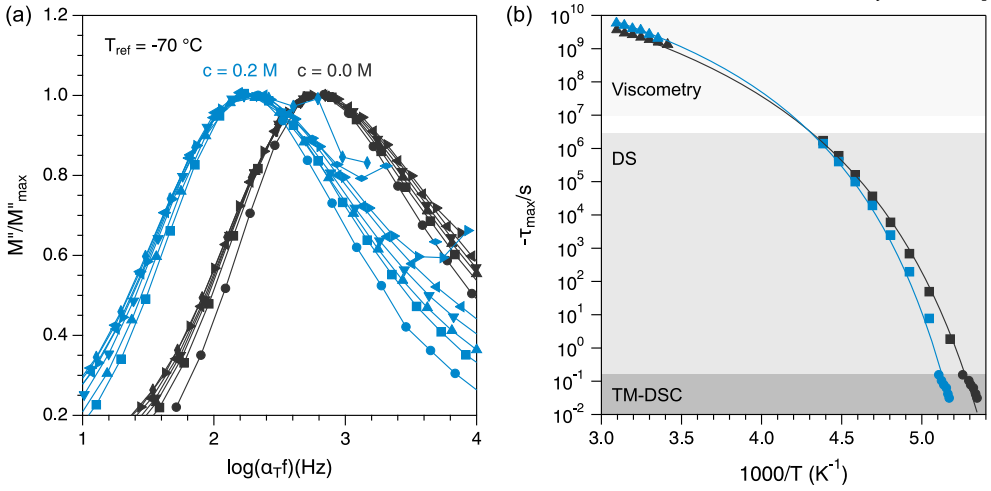

Fig. 11. (a) Normalized M'' spectra horizontally-shifted by an α_T factor for $\chi_{TFSI} = 0.4$ sample at two different Li salt concentration. (b) The characteristic relaxation time (τ_σ) (squares), TM-DSC (circles), and viscosimetry (triangles) data as a function of inverse temperature. The solid lines represent VFT fits.

Table 1
The VFT parameters and dielectric glass transition temperature.

LiTFSI	-logτ_0(K)	B (K)	T_0(K)	T_g (K)
c = 0.0 M	-12	800 ± 20	167.6 ± 0.5	195.6 ± 0.5
c = 0.2 M	-12	970 ± 20	156.6 ± 0.6	186.5 ± 0.5

with f_{max} being the frequency at the peak maximum of M''.

Fig. 11a shows the normalized M'' spectra for the $\chi_{TFSI} = 0.4$ sample, with and without Li salt, horizontally-shifted by an α_T factor based on the frequency-temperature superposition principle [29]. A reference temperature of -70 °C was used for both samples. Upon the addition of salt (c = 0.2 M), the M'' peak shifts to lower frequency, indicating a slowdown in the conductivity. This may be attributed to an increased viscosity, agreeing with previously discussed results.

Moreover, the extracted characteristic relaxation times were correlated with the structural segmental dynamics obtained from viscometry and TM-DSC measurements, as shown in Fig. 11b. The combined data from the three characterization methods fall into a common curve and display a typical Vogel-Fulcher-Tammann (VFT) behavior:

$$\tau_{max} = \tau_0 \cdot exp\left(\frac{B}{T - T_0}\right) \quad (2)$$

where τ_0 is the relaxation time at high temperature, B is a parameter that determines the deviation from the typical Arrhenius temperature dependence, where a lower B value indicates a larger deviation, and T_0 is the Vogel temperature (always lower than T_g).

The VFT data, summarized in Table 1, show good agreement between the sigma-process (characteristic relaxation time τ_σ) and the structural relaxation (T_g related process) for both mixtures, *i.e.*, with and without the addition of Li salt. This confirms that the conductivity process is primarily governed by the viscosity of the solutions.

3.6. Dynamics near the glass transition

Accurate information about the heterogeneous dynamics near T_g was obtained through TM-DSC measurements. This method is based on the concept of cooperatively rearranging regions (CRR), introduced by Adam and Gibbs [30]. A CRR is defined as the smallest volume capable of undergoing structural relaxation independently of its surroundings. The cooperative length scale can be estimated using Donth's theorem [31]:

$$\xi_a = \left(\frac{3k_B T_g^2 \Delta(1/C_p)}{4\pi\rho\delta T^2}\right)^{1/3} \quad (3)$$

where K_B is Boltzmann constant, T_g is the glass transition temperature, C_p is the heat capacity in J/g·K, ρ is the mass density in g/cm^3 and δT^2 is the mean-square temperature fluctuation of one average CRR, functional to the dynamic glass transition.

Fig. 12a illustrates the method used to determine the parameters needed to estimate the cooperative length scale: (*i*) the glass transition temperature, based on the peak of the derivative of the heat flow, and (*ii*) the heat capacity values in the liquid and glassy states. Accordingly, the estimated length scale of dynamic heterogeneity for $\chi_{TFSI} = 0.4$

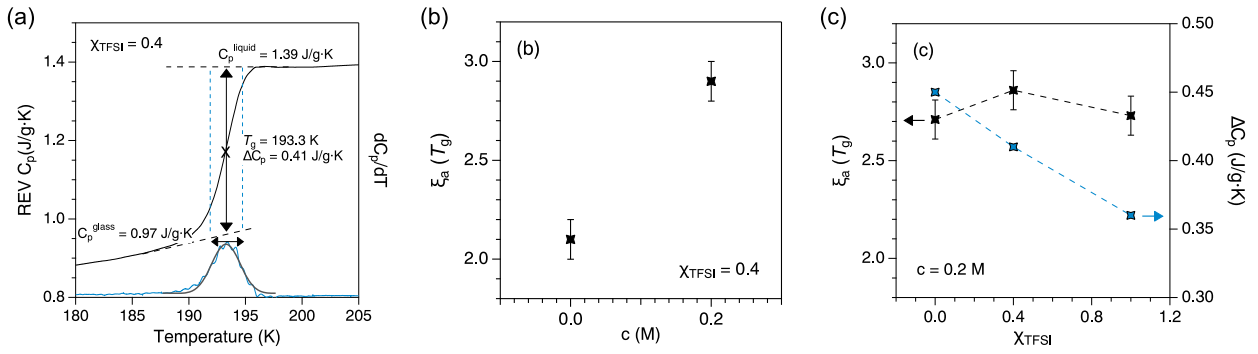

Fig. 12. (a) TM-DSC thermogram for $\chi_{TFSI} = 0.4$. (b) Cooperative length scale as a function of Li salt concentration for $\chi_{TFSI} = 0.4$. (c) Cooperative length scale (black curve) and heat capacity (blue curve) as a function of χ_{TFSI} for 0.2 M LiTFSI solutions.

with and without Li salt, are shown in Fig. 12b. The addition of Li salt leads to an increase in the characteristic length scale, suggesting stronger electrostatic interactions, likely as a result of higher molecular packing. At a concentration of 0.2 M LiTFSI, the heat capacity decreases linearly with increasing χ_{TFSI} while the dynamic heterogeneity remains nearly unchanged, Fig. 12c. This suggests a decrease in the system's degrees of freedom, thus an increase in intermolecular interactions. The analysis of the relaxation dynamics data further supports the previously discussed results, emphasizing the importance of optimizing intermolecular interactions within a system to suppress phase transitions within the operational range, while still ensuring effective ion transport.

4. Conclusion

In this study, mixtures of two protic ionic liquids, [C_2Him][TFSI] and [C_2Him][NO_3], were systematically investigated with and without the addition of 0.2 M LiTFSI to assess their potential as electrolytes for Li-ion batteries. By varying the molar ratio between the two ionic liquids, sharing a common cation but differing in anion size, charge delocalization, and polarity, notable effects on thermal and transport properties were observed. The results demonstrate that both anion mixing and Li-salt addition suppress or hinder phase transitions, thereby expanding the operational temperature window towards the lower temperature range, with the exception of pure [C_2Him][NO_3]. The Walden plot analysis indicates composition-dependent changes in ion association and transport mechanisms, indicating that specific compositions (particularly χ_{TFSI} = 0.2 and 0.4) are optimal for enhanced ionic conductivity. Spectroscopic evidence further revealed preferential interactions between [C_2Him] and [NO_3] anions, resulting in weaker coordination with [TFSI], which explains the observed transport behavior. Overall, the compositional range $0.2 \leq \chi_{TFSI} \leq 0.4$, with or without lithium salt, offers the most favorable combination of wide liquid-phase temperature range and high ionic conductivity. These findings highlight the promise of such mixed protic ionic liquid systems as tunable, efficient electrolytes for energy storage applications.

CRediT authorship contribution statement

Nicole Abdou: Writing – review & editing, Writing – original draft, Visualization, Methodology, Investigation, Formal analysis, Data curation, Conceptualization. **Achilleas Pipertzis:** Writing – review & editing, Validation, Investigation, Formal analysis, Data curation. **Jan Swenson:** Writing – review & editing, Validation, Supervision, Project administration, Funding acquisition. **Anna Martinelli:** Writing – review & editing, Visualization, Validation, Supervision, Project administration, Funding acquisition, Conceptualization.

Declaration of competing interest

The authors declare that they have no known competing financial interests or personal relationships that could have appeared to influence the work reported in this paper.

Acknowledgements

The authors kindly thank the Areas of Advance *Materials Science* and *Energy* at Chalmers University of Technology for the fund. The authors thank Prof. Aleksandar Matic for access to the viscosity and density measurement equipment. The authors thank Prof. Anna Ström and Ratchawit Janewithayapun for the help with rheology measurements. The authors also thank the Swedish NMR Centre (SNC) in Gothenburg for the allocated NMR time.

Appendix A. Supplementary material

Supplementary material related to this article can be found online at https://doi.org/10.1016/j.molliq.2025.128418.

Data availability

Data will be made available on request.

References

[1] T. Vogl, P. Goodrich, J. Jacquemin, S. Passerini, A. Balducci, The influence of cation structure on the chemical–physical properties of protic ionic liquids, J. Phys. Chem. C 120 (16) (2016) 8525–8533, https://doi.org/10.1021/acs.jpcc.6b01945.
[2] Z. Lei, B. Chen, Y.-M. Koo, D.R. MacFarlane, Introduction: ionic liquids, Chem. Rev. 117 (10) (2017) 6633–6635, https://doi.org/10.1021/acs.chemrev.7b00246.
[3] P.I. Walden, Ueber die molekulargrosse und elektrische leitfahigkeit einiger geschmolzenen salze, Bulletin de l'Académie Impériale 413 des Sciences de Saint-Pétersbourg 8 (1914) 405–422, https://doi.org/10.1051/jphystap:018880070017601.
[4] C. Austen Angell, Y. Ansari, Z. Zhao, Ionic liquids: past, present and future, Faraday Discuss. 154 (2012) 9–27, https://doi.org/10.1039/C1FD00112D.
[5] T.L. Greaves, C.J. Drummond, Protic ionic liquids: properties and applications, Chem. Rev. 108 (1) (2007) 206–237, https://doi.org/10.1021/cr068040u.
[6] T.L. Greaves, C.J. Drummond, Protic ionic liquids: evolving structure-property relationships and expanding applications, Chem. Rev. 115 (20) (2015) 11379–11448, https://doi.org/10.1021/acs.chemrev.5b00158.
[7] D.R. MacFarlane, N. Tachikawa, M. Forsyth, J.M. Pringle, P.C. Howlett, G.D. Elliott, J.H. Davis, M. Watanabe, P. Simon, C.A. Angell, Energy applications of ionic liquids, Energy Environ. Sci. 7 (2014) 232–250, https://doi.org/10.1039/C3EE42099J.
[8] M. Watanabe, Design and materialization of ionic liquids based on an understanding of their fundamental properties, Electrochemistry 84 (9) (2016) 642–653, https://doi.org/10.5796/electrochemistry.84.642.
[9] M. Watanabe, M.L. Thomas, S. Zhang, K. Ueno, T. Yasuda, K. Dokko, Application of ionic liquids to energy storage and conversion materials and devices, Chem. Rev. 117 (10) (2017) 7190–7239, https://doi.org/10.1021/acs.chemrev.6b00504.
[10] S. Zhang, J. Zhang, Y. Zhang, Y. Deng, Nanoconfined ionic liquids, Chem. Rev. 117 (10) (2017) 6755–6833, https://doi.org/10.1021/acs.chemrev.6b00509.
[11] M.N. Garaga, V. Dracopoulos, U. Werner-Zwanziger, J.W. Zwanziger, M. Maréchal, M. Persson, L. Nordstierna, A. Martinelli, A long-chain protic ionic liquid inside silica nanopores: enhanced proton mobility due to efficient self-assembly and decoupled proton transport, Nanoscale 10 (2018) 12337–12348, https://doi.org/10.1039/C8NR02031K.
[12] A. Deshpande, L. Kariyawasam, P. Dutta, S. Banerjee, Enhancement of lithium ion mobility in ionic liquid electrolytes in presence of additives, J. Phys. Chem. C 117 (48) (2013) 25343–25351, https://doi.org/10.1021/jp409498w.
[13] P.M. Bayley, A.S. Best, D.R. MacFarlane, M. Forsyth, The effect of coordinating and non-coordinating additives on the transport properties in ionic liquid electrolytes for lithium batteries, Phys. Chem. Chem. Phys. 13 (2011) 4632–4640, https://doi.org/10.1039/C0CP02084B.
[14] F. Lundin, A. Idström, P. Falus, L. Evenäs, S. Xiong, A. Matic, Ion dynamics and nanostructures of diluted ionic liquid electrolytes, J. Phys. Chem. C 126 (38) (2022) 16262–16271, https://doi.org/10.1021/acs.jpcc.2c04503.
[15] M.S. Miran, T. Yasuda, M.A.B.H. Susan, K. Dokko, M. Watanabe, Binary protic ionic liquid mixtures as a proton conductor: high fuel cell reaction activity and facile proton transport, J. Phys. Chem. C 118 (48) (2014) 27631–27639, https://doi.org/10.1021/jp506957y.
[16] I. Abdurrokhman, A. Martinelli, Binary mixtures of imidazolium-based protic ionic liquids. Extended temperature range of the liquid state keeping high ionic conductivities, Front. Chem. 10 (2022) 915683, https://doi.org/10.3389/fchem.2022.915683.
[17] X. Tang, Y. Xu, X. Zhu, Y. Lu, Changes in microstructure of two ammonium-based protic ionic liquids proved by in situ variable-temperature 1h nmr spectroscopy: influence of anion, Magn. Reson. Chem. 56 (2) (2018) 73–79, https://doi.org/10.1002/mrc.4600.
[18] L. Timperman, A. Vigeant, M. Anouti, Eutectic mixture of protic ionic liquids as an electrolyte for activated carbon-based supercapacitors, Electrochim. Acta 155 (2015) 164–173, https://doi.org/10.1016/j.electacta.2014.12.130.
[19] M. Kerner, N. Plylahan, J. Scheers, P. Johansson, Ionic liquid based lithium battery electrolytes: fundamental benefits of utilising both tfsi and fsi anions?, Phys. Chem. Chem. Phys. 17 (2015) 19569–19581, https://doi.org/10.1039/C5CP01891A.
[20] M.A. Navarra, Ionic liquids as safe electrolyte components for li-metal and li-ion batteries, Mater. Res. Soc. Bull. 38 (7) (2013) 548–553, https://doi.org/10.1557/mrs.2013.152.
[21] G. Huang, Y. Liao, X. Zhao, X. Jin, Z. Zhu, M. Guan, Y. Li, Tuning a solvation structure of lithium ions coordinated with nitrate anions through ionic liquid-based solvent for highly stable lithium metal batteries, Adv. Funct. Mater. 33 (6) (2023) 2211364, https://doi.org/10.1002/adfm.202211364.
[22] G. Huang, G. Chen, X. Jin, K. Ge, M. Guan, Y. Li, Enabling uniform li deposition behavior by introducing a no3 – -based ionic liquid additive into carbonate electrolyte for high-voltage li metal batteries, J. Power Sources 556 (2023) 232497, https://doi.org/10.1016/j.jpowsour.2022.232497.
[23] A. Fernicola, B. Scrosati, H. Ohno, Potentialities of ionic liquids as new electrolyte media in advanced electrochemical devices, Ionics 12 (2) (2006) 95–102, https://doi.org/10.1007/s11581-006-0023-5.

[24] E.M. Morais, I. Abdurrokhman, A. Martinelli, Solvent-free synthesis of protic ionic liquids. Synthesis, characterization and computational studies of triazolium based ionic liquids, J. Mol. Liq. 360 (2022) 119358, https://doi.org/10.1016/j.molliq.2022.119358.

[25] S. Kocevska, G.M. Maggioni, S.H. Crouse, R. Prasad, R.W. Rousseau, M.A. Grover, Effect of ion interactions on the Raman spectrum of no3 − : toward monitoring of low-activity nuclear waste at hanford, Chem. Eng. Res. Des. 181 (2022) 173–194, https://doi.org/10.1016/j.cherd.2022.03.002.

[26] Y. Umebayashi, T. Yamaguchi, S. Fukuda, T. Mitsugi, M. Takeuchi, K. Fujii, S.-I. Ishiguro, Raman spectroscopic study on alkaline metal ion solvation in 1-butyl-3-methylimidazolium bis(trifluoromethanesulfonyl)amide ionic liquid, Anal. Sci. 24 (10) (2008) 1297–1304, https://doi.org/10.2116/analsci.24.1297.

[27] M. Herstedt, M. Smirnov, P. Johansson, M. Chami, J. Grondin, L. Servant, J.C. Lassègues, Spectroscopic characterization of the conformational states of the bis(trifluoromethanesulfonyl)imide anion (tfsi −), J. Raman Spectrosc. 36 (8) (2005) 762–770, https://doi.org/10.1002/jrs.1347.

[28] J. Pitawala, A. Martinelli, P. Johansson, P. Jacobsson, A. Matic, Coordination and interactions in a li-salt doped ionic liquid, J. Non-Cryst. Solids 407 (2015) 318–323, https://doi.org/10.1016/j.jnoncrysol.2014.08.043, 7th IDMRCS: Relaxation in Complex Systems.

[29] F. Kremer, A. Schönhals, Broadband Dielectric Spectroscopy, Springer Science & Business Media, 2002.

[30] G. Adam, J.H. Gibbs, On the temperature dependence of cooperative relaxation properties in glass-forming liquids, J. Chem. Phys. 43 (1) (1965) 139–146, https://doi.org/10.1063/1.1696442.

[31] E. Donth, The size of cooperatively rearranging regions at the glass transition, J. Non-Cryst. Solids 53 (3) (1982) 325–330, https://doi.org/10.1016/0022-3093(82)90089-8.